QUANTUM OPTICS

Photon-mediated interactions between quantum emitters in a diamond nanocavity

R. E. Evans[1]*, M. K. Bhaskar[1]*, D. D. Sukachev[1]*, C. T. Nguyen[1], A. Sipahigil[1,2], M. J. Burek[3], B. Machielse[1,3], G. H. Zhang[1], A. S. Zibrov[1], E. Bielejec[4], H. Park[1,5], M. Lončar[3], M. D. Lukin[1]†

Photon-mediated interactions between quantum systems are essential for realizing quantum networks and scalable quantum information processing. We demonstrate such interactions between pairs of silicon-vacancy (SiV) color centers coupled to a diamond nanophotonic cavity. When the optical transitions of the two color centers are tuned into resonance, the coupling to the common cavity mode results in a coherent interaction between them, leading to spectrally resolved superradiant and subradiant states. We use the electronic spin degrees of freedom of the SiV centers to control these optically mediated interactions. Such controlled interactions will be crucial in developing cavity-mediated quantum gates between spin qubits and for realizing scalable quantum network nodes.

Photon-mediated interactions between quantum emitters are an important building block of quantum information systems, enabling entanglement generation and quantum logic operations involving both stationary qubits and photons (*1*, *2*). Progress in cavity quantum electrodynamics (QED) with trapped atoms and ions (*3*), superconducting qubits (*4*), and self-assembled quantum dots (*5*) has created possibilities for engineering such interactions. In particular, coherent multi-qubit interactions mediated via a cavity have been demonstrated in the microwave domain using circuit QED (*6*). Extending such interactions to the optical domain could enable key protocols in long-distance quantum communication (*1*, *7*). This goal is challenging owing to the difficulty of achieving strong cavity coupling and individual control of multiple resonant quantum emitters. Recently, cavity-modified collective scattering has been observed in two-ion (*8*) and two-atom (*9*) systems. Signatures of cavity-mediated interactions between quantum dots have also been reported (*10*, *11*). However, the realization of controlled, coherent optical interactions between solid-state emitters is difficult because of inhomogeneous broadening and decoherence introduced by the solid-state environment (*5*, *11*).

We realize controllable optically mediated interactions between negatively charged silicon-vacancy (SiV) color centers coupled to a diamond photonic crystal cavity (Fig. 1A) (*12*). SiV centers in diamond are atom-like quantum emitters featuring nearly lifetime-limited optical linewidths with low inhomogeneous broadening, both in bulk (*13*) and in nanostructures (*14*). We integrate SiV centers into devices consisting of a one-dimensional diamond waveguide with an array of holes defining a photonic crystal cavity with quality factor $Q \sim 10^4$ and simulated mode volume $V \sim 0.5[\lambda/(n = 2.4)]^3$ (Fig. 1B) (*15*). SiV centers are positioned at a single spot in these devices with 40-nm precision by targeted implantation using a focused beam of ^{29}Si ions, yielding around five SiV centers per device (*12*). The diamond waveguide is tapered and adiabatically coupled to a tapered single-mode fiber, enabling collection efficiencies from the waveguide into the fiber of more than 90% (*15*). These devices are placed in a dilution refrigerator with an integrated confocal microscope (*16*). At 85 mK, SiV centers are completely polarized into the orbital ground state (*17*). Here, we use optical transitions between the lowest-energy orbital states in the electronic ground and excited states. The SiV electronic spin degeneracy is lifted by applying a magnetic field up to 10 kG (*17*, *18*). The cavity resonance frequency ω_c is tuned using gas condensation (*16*).

The coupling between SiV centers and the cavity is characterized by scanning the frequency of a laser incident on one side of the device from free space while monitoring the transmitted intensity in the collection fiber. The resulting transmission spectrum (Fig. 1C) reveals strong modulation of the cavity response resulting from the coupling of spectrally resolved SiV centers to the cavity mode. For instance, two SiV centers near the cavity resonance each result in almost-full extinction of the transmission through the cavity (Fig. 1C, lower spectrum) (*19*). By contrast, when the cavity is detuned from the SiV by several cavity linewidths (κ), the spectrum shows a narrow peak near each SiV frequency (Fig. 1D), corresponding to an atom-like dressed state of the SiV-cavity system with high transmission (*6*). The resonance linewidth (Γ) changes by more than an order of magnitude depending on the SiV-cavity detuning ($\Delta = \omega_c - \omega_{SiV}$). This can be understood through Purcell enhancement, which predicts $\Gamma(\Delta) \approx \gamma + \frac{4g^2}{\kappa}\frac{1}{1+4\Delta^2/\kappa^2}$ where g is the single-photon Rabi frequency, κ is the cavity energy decay rate, and γ is twice the decoherence rate due to free-space spontaneous emission and spectral diffusion. For the strongest-coupled SiV in the device used in Fig. 1, linewidths range from $\Gamma(0) = 2\pi \times 4.6$ GHz on resonance to $\Gamma(7\kappa) = 2\pi \times 0.19$ GHz $\approx \gamma$ when the cavity is far detuned. The measured $\Gamma(0)$ corresponds to an estimated lifetime of 35 ps compared to the natural SiV lifetime of 1.8 ns (*12*). These measurements give cavity QED parameters $\{g, \kappa, \gamma\} = 2\pi \times \{7.3, 48, 0.19\}$ GHz, corresponding to a cooperativity (the key cavity-QED figure of merit) $C = 4g^2/\kappa\gamma \sim 23$ (*16*). This order-of-magnitude improvement in SiV-cavity cooperativity over previous work (*12*, *20*) primarily results from the decreased cavity mode volume (*15*).

As is evident from Fig. 1C, SiV centers are subject to inhomogeneous broadening, resulting predominantly from strain within the device (*14*, *21*). This broadening is smaller than that of other solid-state emitters compared to their lifetime-limited linewidths (*5*, *10*, *11*). Indeed, the frequencies of some SiV centers within the same devices are nearly identical. We study the cavity-mediated interaction between a pair (SiV 1 and SiV 2 in Fig. 1) of such nearly-resonant SiV centers (SiV-SiV detuning $\delta = 2\pi \times 0.6$ GHz) coupled to the cavity in the dispersive regime, that is, with large SiV-cavity detuning ($\Delta = 2\pi \times 79$ GHz $> \kappa$, Fig. 2A). To identify resonances associated with individual SiV centers, we selectively ionize either SiV into an optically inactive charge state by applying a resonant laser at powers orders of magnitude higher than those used to probe the system (*16*). This allows measurement of each of the SiV centers' spectra individually, with the other parameters (such as Δ) fixed (Fig. 2A, gray data).

When both SiV centers are in the optically active charge state, the splitting between the resonances increases. The new resonances (Fig. 2A , black data) also display different amplitudes compared with the single-SiV resonances and are labeled as bright ($|S\rangle$) and dark ($|D\rangle$) states. The linewidths of $|S\rangle$ ($|D\rangle$) are also enhanced (suppressed) compared to those of the individual SiV centers (Fig. 2B , inset). At a cavity detuning of the opposite sign ($\Delta = 2\pi \times -55$ GHz), the sign of the energy splitting δ_{SD} between $|S\rangle$ and $|D\rangle$ is reversed (Fig. 2B) . The observation that Δ affects δ_{SD} indicates that this effect arises from the cavity.

To understand these observations, we describe the system of two SiV centers coupled to a cavity mode using the Hamiltonian (*6*, *22*):

$$\hat{H}/\hbar = \omega_c \hat{a}^\dagger \hat{a} + \omega_1 \hat{\sigma}_1^\dagger \hat{\sigma}_1 + \omega_2 \hat{\sigma}_2^\dagger \hat{\sigma}_2 + \hat{a}^\dagger(g_1\hat{\sigma}_1 + g_2\hat{\sigma}_2) + \hat{a}(g_1^*\hat{\sigma}_1^\dagger + g_2^*\hat{\sigma}_2^\dagger)$$

[1]Department of Physics, Harvard University, Cambridge, MA 02138, USA. [2]Institute for Quantum Information and Matter and Thomas J. Watson, Sr., Laboratory of Applied Physics, California Institute of Technology, Pasadena, CA 91125, USA. [3]John A. Paulson School of Engineering and Applied Sciences, Harvard University, Cambridge, MA 02138, USA. [4]Sandia National Laboratories, Albuquerque, NM 87185, USA. [5]Department of Chemistry and Chemical Biology, Harvard University, Cambridge, MA 02138, USA.
*These authors contributed equally to this work.
†Corresponding author. Email: lukin@physics.harvard.edu

where ω_i is the frequency of the ith SiV center and $\hat{a}$ and $\hat{\sigma}_i$ are the cavity photon annihilation and ith SiV center's electronic state lowering operators. Coherent evolution under $\hat{H}$ is modified by cavity (κ) and SiV (γ) decay and decoherence (*16*). In the dispersive regime, $\hat{H}$ yields an effective Hamiltonian for two resonant ($\delta = 0$) SiV centers (*6*, *22*): $\hat{H}_{\text{eff}}/\hbar = J(\hat{\sigma}_1\hat{\sigma}_2^{+} + \hat{\sigma}_1^{+}\hat{\sigma}_2)$ where $J = \frac{g^2}{\Delta}$ (in our system, $g_1 \approx g_2 \equiv g$). Thus, the two SiV centers undergo a flip-flop interaction at rate J mediated by the exchange of cavity photons (Fig. 2C) . This interaction hybridizes the two SiV centers, forming collective eigenstates from the SiV ground $|g\rangle$ and excited $|e\rangle$ states which, for $\delta = 0$, are $|S\rangle = \frac{1}{\sqrt{2}}(|eg\rangle + |ge\rangle)$ and $|D\rangle = 1/\sqrt{2}(|eg\rangle - |ge\rangle)$ and are split by $2J$ (Fig. 2D) (*6*). The symmetric superradiant state $|S\rangle$ has an enhanced coupling to the cavity of $\sqrt{2}g$ (making it "bright" in transmission) and an energy shift of $2J = 2g^2/\Delta$, whereas the antisymmetric combination $|D\rangle$ is completely decoupled from the cavity ("dark" in transmission) and has zero energy shift (*6*, *11*). As δ/J increases, $|D\rangle$ becomes visible and the individual SiV eigenstates are eventually recovered. The energy shift of state $|S\rangle$ is away from the cavity resonance, explaining the reversed energy difference δ_{SD} upon changing the sign of Δ (Fig. 2B) . By comparing the data in Fig. 2 to theory accounting for finite δ (Fig. 2, solid curves), the SiV-SiV interaction strength $J = 2\pi \times 0.6$ GHz is extracted. The splitting δ_{SD} (which is at least $2J$) is larger than the measured linewidths (for a single SiV, $\Gamma(\Delta = 79\text{ GHz}) = 2\pi \times 0.4$ GHz), allowing these states to be spectrally resolved.

Next, the SiV center's long-lived electronic spin degree of freedom (*18*) is used to control the SiV-cavity transmission and two-SiV interaction. We apply a magnetic field to lift the degeneracy of the spin sublevels in the ground (spinstates $|\uparrow\rangle$ and $|\downarrow\rangle$) and optically excited ($|\uparrow'\rangle$ and $|\downarrow'\rangle$) states. The Zeeman shifts are different for each orbital state and depend on the magnitude and orientation of the field with respect to the SiV center's symmetry axis, yielding spectrally distinguishable spin-selective optical transitions at frequencies $\omega_\uparrow$ and $\omega_\downarrow$ (Fig. 3A). In general, the splitting between these frequencies is maximized for off-axis magnetic fields (*18*). Any off-axis magnetic field also prevents the optical transitions from being perfectly cycling, allowing the SiV center to be initialized into $|\uparrow\rangle$ by pumping at $\omega_\downarrow$ and vice versa (*23*, *24*). Coupling spin-selective transitions to the cavity mode enables high-contrast spin-dependent modulation of the cavity transmission (*25*).

We demonstrate this effect using an SiV center in the dispersive regime ($\Delta \sim 2\kappa$). Here, the optical transition linewidth is narrow, allowing us to resolve these transitions in a 9-kG field well-aligned with the SiV center's symmetry axis where the transitions are highly cycling (branching fraction ~$1 - 10^{-4}$) (*17*). The spin is initialized in $|\downarrow\rangle$ or $|\uparrow\rangle$ via optical pumping, and the system is probed in transmission. When the spin is in $|\downarrow\rangle$, the interaction with the probe at $\omega_\uparrow$ is negligible, and the probe is reflected by the detuned cavity (Fig. 3B, red curve). When the spin is in $|\uparrow\rangle$, single photons at frequency $\omega_\uparrow$ are transmitted via the SiV-like dressed state (blue curve) for a time (12 ms) determined by the cyclicity of the transition (*17*). The distribution of photon counts detected in a 7-ms window when the spin is initialized in $|\downarrow\rangle$ (red) versus $|\uparrow\rangle$ (blue) (Fig. 3C) is well-resolved, allowing the spin state to be determined in a single shot with 97% fidelity (*16*).

We also perform this experiment in the resonant-cavity regime and observe spin-dependent transmission switching with 80% contrast (*16*).

The combination of spin control, high-cooperativity coupling, and a small inhomogeneous distribution of SiVs enables controllable optically mediated interactions between multiple SiV centers. We focus on two SiV centers (SiV 1 and SiV 2 in Fig. 1) in the dispersive

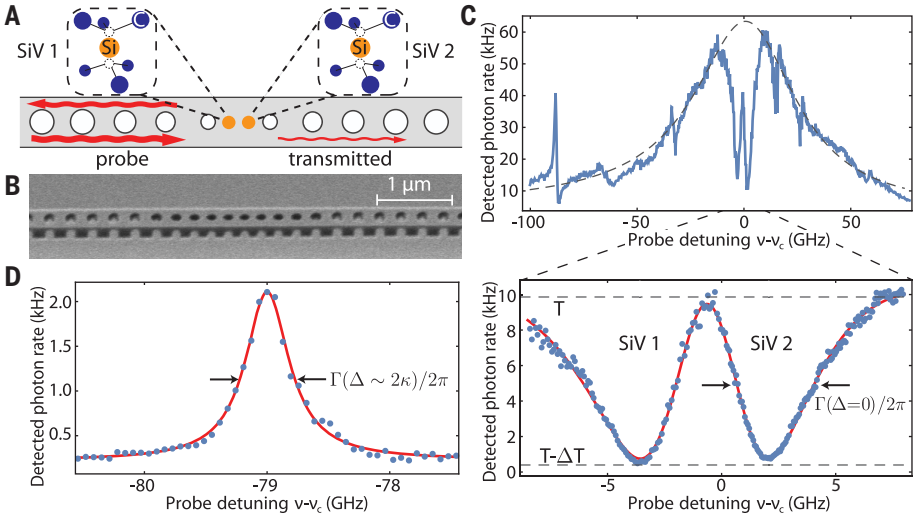

Fig. 1. High cooperativity SiV-photon interface. (**A**) Schematic of a diamond nanocavity containing two SiV centers. (**B**) Scanning electron micrograph of a nanocavity. (**C**) Transmission spectrum of the coupled SiV-cavity system (blue). The broad Lorentzian response of an empty cavity (dashed) is modulated by cavity-coupled SiVs. Near the cavity resonance (lower panel), two SiVs each result in greater than 95% extinction in transmission and are broadened by the Purcell effect [$\Gamma(\Delta = 0) = 2\pi \times 4.6$ GHz]. (**D**) In the dispersive regime ($\Delta = 2\pi \times 79$ GHz ~ 2κ), SiVs appear as narrow peaks in transmission [$\Gamma(\Delta = 2\pi \times 0.5$ GHz]. The solid lines in (D) and the lower panel of (C) are fits to a model (*16*).

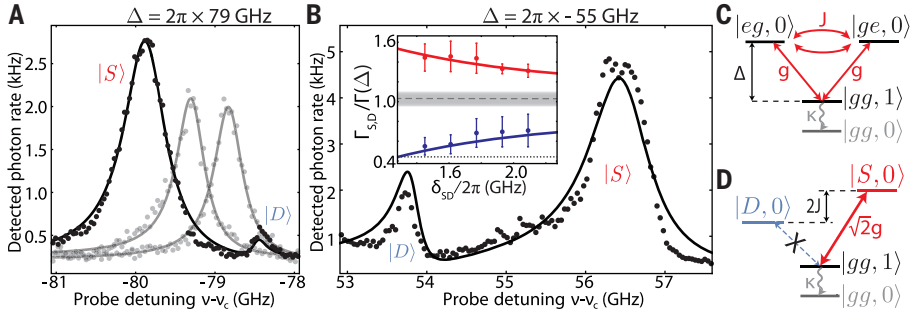

Fig. 2. Cavity mediated SiV-SiV interactions. (**A**) Transmission spectrum of two nearly resonant SiVs ($\delta = 2\pi \times 0.56$ GHz) at cavity detuning ($\Delta = 2\pi \times 79$ GHz). When both SiVs are coupled to the cavity, superradiant (bright) $|S\rangle$ and subradiant (dark) $|D\rangle$ states are formed (black). Spectra of noninteracting SiVs are shown in gray. (**B**) Transmission spectrum of the same SiVs at $\Delta = 2\pi \times -55$ GHz and $\delta = 2\pi \times 2$ GHz. Inset: ratio of $|S\rangle$ (red) and $|D\rangle$ (blue) state linewidths to the single-SiV linewidth at ($\Delta = 2\pi \times 79$ GHz) as a function of δ_{SD}. The resonance frequencies of these SiVs slowly drift as a result of spectral diffusion (*14*), allowing us to measure the linewidths of $|S\rangle$ and $|D\rangle$ at different δ_{SD}. The gray dashed line and shaded region are the average and standard deviation of the single-SiV linewidths. The dotted line corresponds to the SiV linewidth γ without Purcell enhancement, demonstrating that $|D\rangle$ at minimum δ_{SD} is almost completely decoupled from the cavity. Solid lines in (A) and (B) are predictions based on independently-measured SiV parameters (*16*). (**C**) Energy diagram of two SiV centers coupled to a cavity mode. Interaction via exchange of cavity photons at rate $J = g^2/\Delta$ leads to collective $|S\rangle$ and $|D\rangle$ eigenstates (**D**).

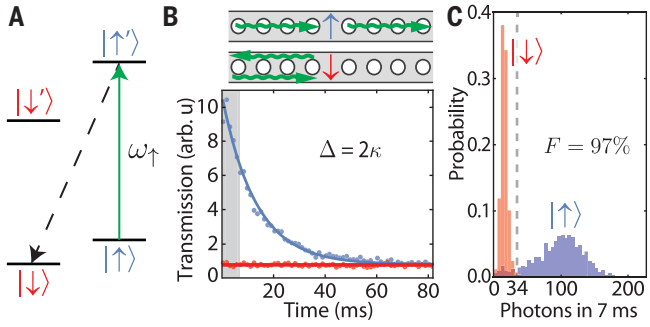

Fig. 3. Cavity-assisted spin initialization and readout. (**A**) Simplified level structure of the SiV in a magnetic field. An optical transition at frequency $\omega_\uparrow$ (green arrow) initializes the SiV spin into $|\downarrow\rangle$ by optical pumping via a spin-flipping transition (dashed line). (**B**) Spin-dependent optical switching in the dispersive regime. State $|\downarrow\rangle$ is not coupled to the probe at frequency $\omega_\uparrow$, which is therefore reflected (red). Initialization into $|\uparrow\rangle$ results in transmission of the probe field (blue). (**C**) Photon number distributions for transmission in the dispersive regime for initialization into $|\uparrow\rangle$ (blue) and $|\downarrow\rangle$ (red) are well-resolved (mean $n_\uparrow = 96$, $n_\downarrow = 16$) in a 7-ms window [gray region in (C)], demonstrating single-shot spin-state readout with 97% fidelity.

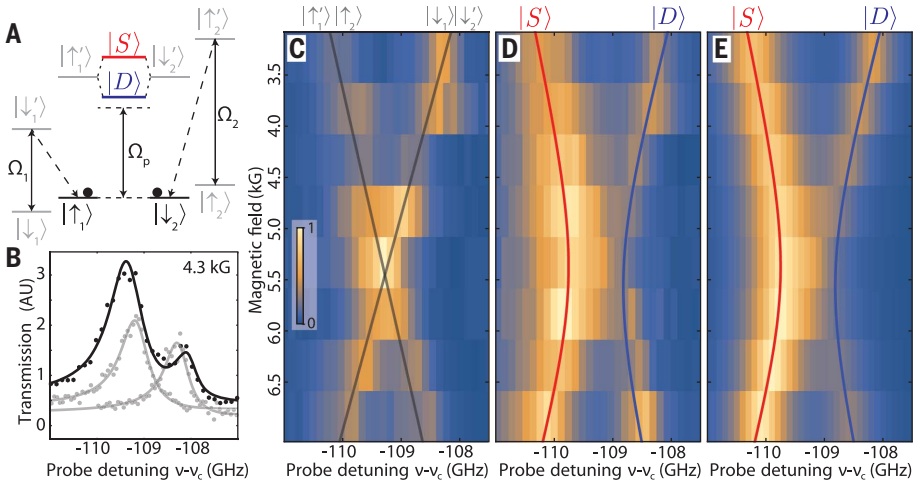

Fig. 4. Deterministic control of photon-mediated interactions via SiV spin states. (**A**) Energy diagram of two SiV centers in a magnetic field. The spins can be initialized in $|\uparrow_1\rangle|\downarrow_2\rangle$ with Ω_1 and Ω_2 and probed by sweeping Ω_p. When Ω_1 (Ω_2) is off, Ω_p is sufficiently strong to ensure initialization in $|\downarrow_1\rangle$ ($|\uparrow_2\rangle$) as it sweeps across the relevant SiV 1 (2) transition. (**B**) Spin-dependent transmission spectra at 4.3 kG. Gray: Spectra of single SiVs in the noninteracting combinations of spin states. Black: Spectrum of two interacting SiVs, demonstrating formation of $|S\rangle$ and $|D\rangle$. (**C**) Composite spectrum of the system at different two-SiV detunings, demonstrating a level crossing characteristic of noninteracting systems. The solid lines are the fitted single-SiV energies of $|\uparrow_1'\rangle|\uparrow_2\rangle$ and $|\downarrow_1\rangle|\downarrow_2'\rangle$ as a function of magnetic field. (**D**) An avoided crossing is visible in cavity transmission when the spins are prepared in the interacting state $|\uparrow_1\rangle|\downarrow_2\rangle$. (**E**) Predicted spectrum. The red and blue lines in (D) and (E) are predicted energies of $|S\rangle$ and $|D\rangle$ (*16*).

regime ($\Delta = 2\pi \times 109$ GHz) with $\{g1 \approx g_2, \kappa, \gamma_1 \approx \gamma_2\} = 2\pi \times \{7.3, 39, 0.5\}$ GHz ($C \approx 11$) and an initial two-SiV detuning $\delta = 2\pi \times 5$ GHz (*16*). We sweep the magnitude of a magnetic field oriented almost orthogonal to the SiV symmetry axis and tune transitions $|\uparrow_1\rangle \rightarrow |\uparrow_1'\rangle$ and $|\downarrow_2\rangle \rightarrow |\downarrow_2'\rangle$ (which have opposite Zeeman shifts) in and out of resonance (Fig. 4A). At each magnetic field, a continuous field Ω_1 or Ω_2 is used to optically pump either SiV 1 or SiV 2 into the spin state resonant with a weak probe field Ω_p measuring the transmission spectrum of the system, thus enabling control measurements where only one spin is addressed by Ω_p at a time (Fig. 4B, gray). The single-spin transmission spectra at each field are summed to form a composite spectrum of the two-SiV system (Fig. 4C), which displays an energy level crossing of the two SiV transitions characteristic of noninteracting systems.

Measurements were then made in the interacting regime by preparing the spins into $|\uparrow_1\rangle|\downarrow_2\rangle$ by simultaneously applying Ω_1 and Ω_2. The two-SiV transmission spectrum demonstrates the formation of superradiant and subradiant states (Fig. 4B, black) that exist only for this combination of spin states. Spectra as a function of applied magnetic field (Fig. 4D) demonstrate an avoided crossing arising from spin-dependent interactions between the two SiV centers (*6*). These experimental observations agree with an analysis based on a complete microscopic model of the system (*16*) including independently measured SiV-cavity parameters (Fig. 4E). For these experiments (Fig. 4), an active preselection sequence is used to stabilize the SiV spectral positions (*16*). Similar observations were reproduced in a separate device on the same chip (*16*).

This optically mediated interaction between quantum emitters could be used to realize key quantum information protocols, including cavity-assisted entanglement generation (*2*, *7*, *22*), efficient Bell-state measurements (*19*, *26*), and robust gates between emitters in distant cavities (*1*). To implement these schemes with high fidelity, qubits should be encoded in long-lived electronic spin states. Recent work has demonstrated that the SiV spin can be used as a long-lived quantum memory (*17*) that can be manipulated with microwave (*17*, *27*) and optical fields (*28*). Although the present work relies on magnetic field tuning of the SiV frequencies, recently developed techniques that include strain (*21*) or Raman tuning (*12*) can be applied to individual devices, allowing our approach to be extended to the chip scale. The infidelity associated with many deterministic cavity-mediated operations scales as $C^{-1/2}$ (*26*) or C^{-1} (*7*) and can therefore be mitigated with improved cooperativity. Although the cooperativity $C \sim 20$ achieved here is among the largest demonstrated in the optical domain, it can be improved by at least an order of magnitude by increasing the cavity Q/V and by reducing sources of spectral diffusion limiting γ (*16*). Alternatively, the cooperativity could be enhanced by using different quantum emitters, such as the GeV (*29*) or SnV (*30*) centers in diamond with higher quantum efficiencies (*29*). Near-unity fidelities can also be achieved with existing cooperativities using heralded schemes where errors can be suppressed via error detection with an auxiliary qubit (*26*). Furthermore, our system could be used to efficiently generate nonclassical states of light (*31*), which are useful in, for example, measurement-based quantum computing. On-chip integration and GHz-level bandwidths make our system well-suited for exploring potential applications in quantum networking, including the implementation of efficient quantum repeaters (*26*) and distributed quantum computing.

REFERENCES AND NOTES

1. J. I. Cirac, P. Zoller, H. J. Kimble, H. Mabuchi, *Phys. Rev. Lett.* **78**, 3221–3224 (1997).
2. A. Imamoğlu *et al.*, *Phys. Rev. Lett.* **83**, 4204–4207 (1999).
3. S. Welte, B. Hacker, S. Daiss, S. Ritter, G. Rempe, *Phys. Rev. X* **8**, 011018 (2018).
4. A. Wallraff *et al.*, *Nature* **431**, 162–167 (2004).
5. P. Lodahl, S. Mahmoodian, S. Stobbe, *Rev. Mod. Phys.* **87**, 347–400 (2015).
6. J. Majer *et al.*, *Nature* **449**, 443–447 (2007).
7. M. J. Kastoryano, F. Reiter, A. S. Sørensen, *Phys. Rev. Lett.* **106**, 090502 (2011).
8. B. Casabone *et al.*, *Phys. Rev. Lett.* **114**, 023602 (2015).
9. R. Reimann *et al.*, *Phys. Rev. Lett.* **114**, 023601 (2015).
10. A. Laucht *et al.*, *Phys. Rev. B* **82**, 075305 (2010).
11. H. Kim, D. Sridharan, T. C. Shen, G. S. Solomon, E. Waks, *Opt. Express* **19**, 2589–2598 (2011).
12. A. Sipahigil *et al.*, *Science* **354**, 847–850 (2016).
13. A. Sipahigil *et al.*, *Phys. Rev. Lett.* **113**, 113602 (2014).
14. R. E. Evans, A. Sipahigil, D. D. Sukachev, A. S. Zibrov, M. D. Lukin, *Phys. Rev. Appl.* **5**, 044010 (2016).

15. M. J. Burek *et al*., *Phys. Rev. Appl.* **8**, 024026 (2017).
16. Materials and methods are available as supplementary materials online.
17. D. D. Sukachev *et al*., *Phys. Rev. Lett.* **119**, 223602 (2017).
18. C. Hepp *et al*., *Phys. Rev. Lett.* **112**, 036405 (2014).
19. E. Waks, J. Vuckovic, *Phys. Rev. Lett.* **96**, 153601 (2006).
20. J. L. Zhang *et al*., *Nano Lett.* **18**, 1360–1365 (2018).
21. S. Meesala *et al*., *Phys. Rev. B* **97**, 205444 (2018).
22. S.-B. Zheng, G.-C. Guo, *Phys. Rev. Lett.* **85**, 2392–2395 (2000).
23. L. J. Rogers *et al*., *Phys. Rev. Lett.* **113**, 263602 (2014).
24. B. Pingault *et al*., *Phys. Rev. Lett.* **113**, 263601 (2014).
25. A. Javadi *et al*., *Nat. Nanotechnol.* **13**, 398–403 (2018).
26. J. Borregaard, P. Kómár, E. M. Kessler, M. D. Lukin, A. S. Sørensen, *Phys. Rev. A* **92**, 012307 (2015).
27. B. Pingault *et al*., *Nat. Commun.* **8**, 15579 (2017).
28. J. N. Becker *et al*., *Phys. Rev. Lett.* **120**, 053603 (2018).
29. M. K. Bhaskar *et al*., *Phys. Rev. Lett.* **118**, 223603 (2017).
30. T. Iwasaki *et al*., *Phys. Rev. Lett.* **119**, 253601 (2017).
31. S. E. Economou, N. Lindner, T. Rudolph, *Phys. Rev. Lett.* **105**, 093601 (2010).

ACKNOWLEDGMENTS

We thank D. Twitchen and M. Markham from Element Six for substrates, J. Borregaard and K. De Greve for discussions, and D. Perry for implantation assistance. **Funding:** Support was provided by the NSF, CUA, DoD/ARO DURIP, AFOSR MURI, ONR MURI, ARL, Vannevar Bush Faculty Fellowship, DoD NDSEG (M. K. B.), and NSF GRFP (B. M. and G. Z.). Devices were fabricated at the Harvard CNS (NSF ECCS-1541959). Implantation was performed at Sandia National Laboratories through the Center for Integrated Nanotechnologies, operated for the DOE-SC (contract DE-NA-0003525) by Sandia Corporation, a Honeywell subsidiary. **Author contributions:** R.E., M.K.B., D.S., C.N., and A.S. performed experiments and analyzed data. M.J.B. and B.M. designed and fabricated nanocavities. A.Z. and G.Z. assisted with experiments. E.B. perfomed implantation. H.P., M.L., and M.D.L. supervised experiments and analysis. All authors contributed to analysis and manuscript preparation. **Competing interests:** The authors declare no competing interests. The views expressed here do not necessarily represent the DOE or U.S. Government. **Data and materials availability:** All data are available in the manuscript or supplementary materials.

SUPPLEMENTARY MATERIALS

www.sciencemag.org/content/362/6415/662/suppl/DC1
Materials and Methods
Figs. S1 to S9
References (*32*–*36*)

26 June 2018; accepted 3 September 2018
Published online 20 September 2018
10.1126/science.aau4691